

 Open access • Posted Content • DOI:10.1101/050856

Imaging decision-related neural cascades in the human brain — Source link

Jordan Muraskin, Truman R. Brown, Jennifer M. Walz, Bryan Conroy ...+2 more authors

Institutions: Columbia University, Medical University of South Carolina, Florey Institute of Neuroscience and Mental Health, Philips ...+1 more institutions

Published on: 04 May 2016 - bioRxiv (Cold Spring Harbor Laboratory)

Topics: Functional magnetic resonance imaging and Electroencephalography

Related papers:

- [How do neural processes give rise to cognition? Simultaneously predicting brain and behavior with a dynamic model of visual working memory.](#)
- [Guest Editorial Special Issue on Neural Systems Engineering and Mathematical Modeling of Brain Dynamics Using ECoG/EEG/MEG Oscillations and Machine Learning Methods](#)
- [Cortical network dynamics of perceptual decision-making in the human brain](#)
- [Repetition suppression: a means to index neural representations using BOLD?](#)
- [Cortical response to naturalistic stimuli is largely predictable with deep neural networks](#)

Share this paper:    

View more about this paper here: <https://typeset.io/papers/imaging-decision-related-neural-cascades-in-the-human-brain-45fgvgsazq>

1 Title: **Imaging decision-related neural cascades in the human brain**

2

3 Authors: Jordan Muraskin¹, Truman R. Brown², Jennifer M. Walz³, Bryan Conroy⁴,

4 Robin I. Goldman⁵, Paul Sajda¹

5 ¹ Department of Biomedical Engineering, Columbia University, New York, NY, USA

6 10027

7 ² Center for Biomedical Imaging, Medical University of South Carolina, Charleston, SC,

8 USA, 29425

9 ³ Florey Institute of Neuroscience and Mental Health, Melbourne, Australia

10 ⁴ Philips Research, New York, NY,

11 ⁵ Center for Healthy Minds, University of Wisconsin-Madison, Madison, WI, USA,

12 53705

13

14 Corresponding Author: Paul Sajda, psajda@columbia.edu

15

16

17

18

19

20 ***Abstract***

21 Perceptual decisions depend on coordinated patterns of neural activity cascading across
22 the brain, running in time from stimulus to response and in space from primary sensory
23 regions to the frontal lobe. Measuring this cascade and how it flows through the brain is
24 key to developing an understanding of how our brains function. However observing, let
25 alone understanding, this cascade, particularly in humans, is challenging. Here, we report
26 a significant methodological advance allowing this observation in humans at
27 unprecedented spatiotemporal resolution. We use a novel encoding model to link
28 simultaneously measured electroencephalography (EEG) and functional magnetic
29 resonance imaging (fMRI) signals to infer the high-resolution spatiotemporal brain
30 dynamics taking place during rapid visual perceptual decision-making. After
31 demonstrating the methodology replicates past results, we show that it uncovers a
32 previously unobserved sequential reactivation of a substantial fraction of the pre-response
33 network whose magnitude correlates with decision confidence. Our results illustrate that
34 a temporally coordinated and spatially distributed neural cascade underlies perceptual
35 decision-making, with our methodology illuminating complex brain dynamics that would
36 otherwise be unobservable using conventional fMRI or EEG separately. We expect this
37 methodology to be useful in observing brain dynamics in a wide range of other mental
38 processes.

39

40

41 ***Introduction***

42 The detailed spatiotemporal brain dynamics that underlie human decision-making are
43 difficult to measure. Invasive techniques with sufficient temporal or spatial resolution,
44 such as depth electrodes or cortical arrays used with epilepsy patients, are only feasible in
45 rare cases and, in addition, do not capture activity from the entire brain. In comparison,
46 non-invasive measures such as electroencephalography (EEG) and
47 magnetoencephalography (MEG) suffer from poor spatial resolution, and blood oxygen
48 level dependent functional MRI (BOLD fMRI) from poor temporal resolution and
49 indirect coupling to neural activity (e.g. fMRI)¹. In spite of this, EEG, MEG, and fMRI
50 have been used individually to study perceptual decision-making in the human brain,
51 although, by themselves they provide a limited view of the underlying brain dynamics².

52 Recently, methods enabling simultaneous acquisition of EEG and fMRI
53 (EEG/fMRI) have led to varied analytic approaches aimed at integrating the
54 electrophysiological and hemodynamic information contained in the joint measurements.
55 Such approaches offer the potential to provide a comprehensive picture of global brain
56 dynamics, and will likely offer new insights into how the brain makes rapid decisions^{3,4}.
57 Some of the techniques that have been proposed for combining multi-modal brain signals
58 have separately analyzed the EEG and fMRI data and subsequently juxtaposed the
59 results^{5,6}, while others attempt for a truly integrated approach in order to fully exploit the
60 joint information contained in the data sets⁷. In general, simultaneous EEG/fMRI and the
61 associated analysis techniques have been used to identify neuronal sources of EEG trial-
62 to-trial variability, linking them to cognitive processes such as attention⁸ and inhibition⁹.

63 Many previous studies have used known EEG markers (P1, N2, N170, P300, α -
64 rhythm) or data driven approaches such as Independent Component Analysis (ICA) to
65 combine EEG with fMRI data^{4,8-16}. One promising approach has been to use supervised
66 machine-learning techniques (e.g. classifiers) to find relevant projections of the EEG
67 data, where single-trial variability of the electrophysiological response along these
68 projections can be correlated in the fMRI space. Goldman, et al.¹⁷, Walz, et al.¹⁸ and
69 Fouragnan, et al.¹⁹ have demonstrated this technique on visual and auditory paradigms.
70 This methodology has been shown to localize cortical regions that modulate with the task
71 while preserving the temporal progression of task-relevant neural activity.

72 Here we combine a classification methodology with an encoding model that
73 relates the trial-to-trial variability in the EEG to what is observed in the simultaneously
74 acquired fMRI. Encoding models have become an important machine learning tool for
75 analysis of neuroimaging data, specifically fMRI²⁰. In most cases encoding models have
76 been used to learn brain activity that encodes or represents features of a stimulus, such as
77 visual orientation energy in an image/video²¹⁻²³, acoustic spectral power in sound/speech
78²⁴, or visual imagery during sleep²⁵. In the method presented here, we employ an
79 encoding model to directly relate the simultaneously collected data from the two
80 neuroimaging modalities—instead of features derived from the stimulus, they are derived
81 from EEG component trial-to-trial variability. Specifically, we learn an encoding in the
82 spatially precise fMRI data from the temporally precise trial-to-trial variability of EEG
83 activity predictive of the level of stimulus evidence. This approach leverages the fact that
84 the level of stimulus evidence, as measured via EEG, persists across the trial^{26,27}, and

85 that by discriminating this information in a time-localized way, one can temporally “tag”
86 specific cortical areas by their trial-to-trial variability.

87 Using our framework for learning the BOLD signal encoding of task-relevant and
88 temporally precise EEG component variability, we unravel the cascade of activity from
89 the representation of sensory input to decision formation, decision action, and decision
90 monitoring. A particularly novel finding is that after the activation of decision
91 monitoring regions (i.e. ACC), we see a reactivation of pre-response networks, where the
92 strength of this reactivation correlates with measures of decision confidence. This
93 specific reactivation, as well as the entire spatio-temporal cascade, is completely
94 unobservable using conventional fMRI-only or EEG-only methodologies.

95

96 ***Results***

97 In this study, we used a visual alternative forced choice (AFC) task where
98 subjects were shown brief presentations of pictures corrupted by noise and instructed to
99 rapidly discriminate between object categories. On any given trial, the level of noise, or
100 stimulus evidence, was varied randomly. The task itself, as well as similar visual
101 decision-making tasks²⁸, is believed to engage an extensive set of cortical areas in a
102 coordinated fashion, including regions that are responsible for sensory encoding,
103 evidence accumulation, decision formation, and response and decision monitoring.
104 However, the dynamic interplay of these regions has never been observed in humans.
105 Here we exploit previously reported findings regarding the sensitivity of the EEG and
106 fMRI signals to the level of stimulus evidence during a perceptual decision-making task.
107 Specifically, previous work has shown differential neural responses to high vs. low

108 stimulus evidence in trial averaged EEG event-related potentials (ERPs), where this
109 difference persists across the trial^{26,27}. Similarly, fMRI studies have shown that for
110 perceptual decision making tasks a number of spatially-distributed cortical areas
111 significantly correlate with the level of stimulus evidence^{29,30}. We leverage the fact that
112 the level of stimulus evidence is expressed temporally in the EEG and spatially in the
113 fMRI to “tag” voxels with a time. Specifically, using a classification methodology (i.e.
114 discriminative components) we identify temporally precise expressions of the level of
115 stimulus evidence that then can be spatially localized through an encoding model of the
116 fMRI BOLD data.

117 We collected simultaneous EEG/fMRI data from 21 subjects as they performed a
118 3-AFC task discriminating between faces, cars, and houses (Fig. 1A). Subjects were
119 instructed to discriminate the object class after briefly viewing an image corrupted by
120 varying levels of noise (Fig. 1B) and respond by pressing one of three buttons. Overall,
121 subjects responded with accuracies of $94 \pm 5\%$ and $58 \pm 12\%$ and with response times of
122 $634 \pm 82\text{ms}$ and $770 \pm 99\text{ms}$ for high and low stimulus evidence trials, respectively (Fig.
123 1 C, D). Subject accuracies and response times across stimulus types (faces, cars, houses)
124 for low stimulus evidence trials were similar; however, for high stimulus-evidence trials
125 subject accuracies were higher and response times were shorter for faces than for cars or
126 houses (See Supplemental Information Fig. S1).

127

128 *GLM based analysis of BOLD fMRI shows superposition of cortical areas correlated*
129 *with stimulus evidence*

130 A traditional general linear model (GLM) analysis of the fMRI (see Methods)
131 revealed differences in BOLD activation between the two stimulus evidence conditions
132 (Fig. 1F, SI Table 1). Brain regions showing greater BOLD activation to high vs. low
133 stimulus evidence trials included areas associated with early visual perception and the
134 default mode network²⁶, such as fusiform gyrus, parahippocampal gyrus, lateral occipital
135 cortex, superior frontal gyrus, and posterior cingulate cortex. Regions with greater BOLD
136 activation to low vs. high stimulus evidence trials included areas in the executive control
137 and difficulty networks: such as dorsal lateral prefrontal cortex, anterior cingulate cortex,
138 intraparietal sulcus, and insula. Overall, these GLM results for the BOLD data
139 reproduced previous results in the literature where similar stimuli and paradigms were
140 used²⁹ (Fig. S2A).

141

142 *Extracting temporally localized EEG signatures of stimulus evidence variability*

143 The traditional fMRI results showed multiple brain regions correlated with the
144 difficulty, or stimulus evidence, of the trial; however, this traditional approach does not
145 enable one to infer the relative timing of these fMRI activations. To infer timing at a
146 scale of tens of milliseconds, we used linear classification^{31,32} of the EEG to extract trial-
147 to-trial variability related to stimulus evidence at specified post-stimulus time points.

148 The basic idea is illustrated in Figure 2, where hypothetical neural activity is
149 shown for two different regions that are constituents of the perceptual decision-making
150 network. Averaging over trials would clearly reveal a difference in the mean neural
151 activity between high and low stimulus evidence. However, the two regions contribute
152 differentially to the network, with one region encoding the stimulus evidence (Region 1)

153 and the other integrating it over time (Region 2); both are sensitive to the level of
154 stimulus evidence, though varying so at different times in the trial. By taking
155 advantage of this sensitivity to the stimulus evidence, we can learn EEG discriminant
156 components, i.e. spatial filters, that best classify trials at different time windows given the
157 neural data. We used the trial-to-trial variability along these component directions as
158 features to uniquely tag fMRI voxels with the specific time window of the component.
159 This tagging is done by building an encoding model of the features, given the BOLD
160 signal, details of which are described in the following section.

161 We constructed EEG components by learning linear classifiers at 25ms steps,
162 starting from stimulus onset to 50ms past the average low stimulus evidence response
163 time. We chose a time step of 25ms due to an empirical analysis showing a half width of
164 50ms in the temporal autocorrelation of the EEG data, though in principle this
165 methodology allows for temporal resolution up to the EEG sampling rate. Each classifier
166 was associated with a set of discriminant values, which can be represented as a vector y_{τ} ;
167 each element of the vector is the distance of a given trial to the discrimination boundary
168 for the classifier at time step τ (Fig. 2). This distance can be interpreted as a measure of
169 the EEG classifier's estimate of the level of stimulus evidence for that trial^{17,18,31-34}.

170 Results of the EEG analysis show discriminating information for stimulus
171 evidence spanning the trial (see Fig. 4A), beginning roughly 175ms post-stimulus to past
172 the average response times. A dip occurs around 300ms, indicating stimulus evidence is
173 less discriminative at this time and serves to demarcate early and late cognitive processes.
174 The early process corresponded to the time of the D220 ERP component, which has been
175 shown to modulate with the degree of task difficulty, whether via stimulus noise or task

176 demands³⁵. The later and more prolonged component is likely related to more complex
177 cognitive and motor preparatory processes that differ between high and low stimulus
178 evidence trials. Importantly, although the early and late EEG components were both
179 discriminative, we found their trial-to-trial variability to be uncorrelated (Figs. 4B and
180 S3E), indicating that while the discriminating information (level of stimulus evidence)
181 persists across the trial, it couples differently to processes across time.

182

183 *An encoding model links fMRI activations with temporally distinct EEG trial-to-trial*
184 *variability*

185 After extracting the trial-to-trial variability from the EEG discriminant
186 components, feature vectors y_{τ} are collected across time steps, τ , along with a response
187 time vector to construct a matrix Y . This matrix is the temporally precise representation
188 of the trial-to-trial EEG variability that reflects high vs. low stimulus evidence. An
189 encoding model is then fit, namely a model in which weights are estimated for each time-
190 localized EEG window, to predict the trial-to-trial variability of the BOLD response for
191 each fMRI voxel. Figure 3 shows a schematic of the encoding model framework we used
192 and compares it to a traditional encoding model constructed by using features derived
193 directly from the stimulus. Rather than constructing a map that directly relates each voxel
194 to a type of stimulus feature, such as whether it encodes edges, motion or some semantic
195 concept such as “animal”^{21-23,36-38}, our model is used to construct maps that label voxels
196 by the time window of the variability they encode – i.e. it “tags” each voxel with a
197 “time”, or set of times, when it encodes the variability in the given EEG discriminant
198 component(s).

199 It is important to note that this approach does not attempt to improve source
200 localization typically done for EEG/MEG studies. Our approach instead provides the
201 temporal resolution of EEG (ms) and the spatial resolution of fMRI (mm) without the
202 need to solve the ill-posed inverse solution and make the many associated assumptions
203 required for reliable source-localization results³⁹.

204 An example of the quality of the encoding model is shown in Fig. 4C (see also
205 Fig. S2B) where significant voxels from the encoding model are shown in yellow. Fig.
206 4D shows the trial-to-trial variability of BOLD signal at a specific voxel, comparing it to
207 the variability predicted by the encoding model. Additional validity of the encoding
208 model and single subject results are presented in the Supplemental Information (Fig.
209 S4A/B). The encoding model was also evaluated as a decoding model (see Methods) with
210 the BOLD activity used to predict the trial-to-trial variability in the EEG for unseen
211 data—data on which the encoding model was not trained. Fig. 4E shows these results,
212 expressed as the correlation between the measured and predicted EEG trial-to-trial
213 variability across the 800ms epoch. The shape of the curve is highly consistent with that
214 observed for the EEG data itself (comparing Fig. 4A and Fig. 4E) (additional analysis of
215 the fidelity of the model is provided in the SI, Fig. S3).

216 Given the encoding model, we unwrap the BOLD activity across time by
217 identifying weights that are consistent across subjects in space and time (see Methods).
218 Fig. 5 shows these results for a group level analysis. We observe a progression of activity
219 (see Movie S1), at 25ms resolution, which proceeds simultaneously down the dorsal and
220 ventral streams of visual processing for the first 250ms. After that the cascade becomes
221 more complex with activation in the IPS at 425ms and 750ms (see Fig. 6A), reactivation

222 of the SPL at 675ms and activation of ACC at 600ms along with other regions found in
223 the traditional fMRI results. (see Fig. S5, Tables S2 and an additional analysis using
224 dynamic causal modeling⁴⁰). The reactivation pattern is particularly significant since it
225 would not be observable via a traditional fMRI general linear model (GLM) analysis,
226 which integrates over time and thus superimposes these activities. For example, the
227 changing sign of the middle temporal gyrus (MT) encoding weights in Fig. 6A
228 manifested as no activity in the MT for the traditional fMRI GLM analysis—the change
229 in sign canceled the effective correlation in the GLM (see Fig. 1F and Fig. S1). The areas
230 of activation we find are consistent with previous reports in the literature for human
231 subjects^{29,30}; however, here we are able to link activations across time in a way that was
232 previously only possible with invasive techniques.

233

234 *Cortical reactivation correlates with decision confidence*

235 Further analysis of the spatiotemporal dynamics (see Fig. 6B), shows that the
236 reactivation pattern in the network occurs after decision-monitoring areas become
237 engaged (i.e. after ACC). Spontaneous reactivation, or “replay”, of neural activity in the
238 human brain has been observed and believed to be important for memory consolidation⁴¹
239 and more recently has been hypothesized to play a role in perceptual decision-making by
240 enabling the formation of decision confidence⁴². To test the hypothesis that the
241 reactivation activity we see is in fact related to decision confidence, we used a
242 hierarchical drift diffusion model (DDM)^{43,44} to fit the behavioral data for high and low
243 stimulus evidence conditions (see Methods). Specifically, our model enables us to define
244 a proxy for decision confidence based on the DDM fits to the behavior^{45,46}. Correlating

245 the reactivation level to this confidence proxy shows a strong and significant monotonic
246 relationship between confidence and the level of reactivation (high stimulus evidence-
247 slope= 0.037 ± 0.008 , $t=4.657$, $p=3.2 \times 10^{-6}$; low stimulus evidence-slope= 0.062 ± 0.008 ,
248 $t=7.754$, $p=8.88 \times 10^{-15}$), with low stimulus evidence trials reactivated more strongly than
249 high stimulus evidence trials (difference in slopes= -0.025 ± 0.011 , $t=2.189$, $p=0.029$)(see
250 Fig. 7 and Fig. S7). Additionally, reactivation amplitude correlates with behavioral
251 accuracy (Fig. S8) (high stimulus evidence, slope= 0.0115 ± 0.0047 , $t=2.41$, $p=0.016$; low
252 stimulus evidence, slope= 0.0104 ± 0.0047 , $t=2.19$, $p=0.028$). Recursive feature elimination
253 showed that the IPS/SPL and dorsal lateral prefrontal cortex (DLPFC) clusters
254 contributed the most to reactivation/confidence proxy correlation (Fig. 7C).

255

256

257 ***Discussion***

258 We have shown that linking simultaneously acquired EEG and fMRI using a novel
259 encoding model enables imaging of high-resolution spatiotemporal dynamics that
260 underlie rapid perceptual decision-making — decisions made in less than a second. This
261 method, which resolves whole-brain activity with EEG-like temporal resolution, was
262 shown to uncover reactivation processes that would otherwise be masked by the temporal
263 averaging and slow dynamics of traditional fMRI. More broadly, our results
264 demonstrated a general non-invasive data-driven methodology for measuring high
265 spatiotemporal latent neural processes underlying human behavior.

266 This approach temporally “tags” the BOLD fMRI data by encoding the trial-to-
267 trial variability of the temporally precise task relevant components in simultaneously

268 acquired EEG. In effect, the EEG discrimination indexes the activity of interest at high
269 temporal resolution, defining a feature space, and the trial-to-trial variability of these
270 discriminant components becomes the specific feature values used in the encoding model.
271 For the case presented here, this variability was used to tease apart the cascade of activity
272 modulated by stimulus evidence across the trial, and this allowed us to observe, as never
273 seen before, the spatiotemporal brain dynamics underlying a perceptual decision.

274 Previous studies have sought to generalize the timing diagram of a perceptual
275 decision through multi-unit recordings in non-human primates^{47,48} or more broadly in
276 humans^{29,30} using fMRI. Our results confirmed the general temporal ordering of
277 activations found previously (early visual processing, decision formation, decision
278 monitoring). However, there was a possibility the temporal order we observed using our
279 technique was an artifact of our methodology. To assess this possibility, we performed
280 additional analyses using dynamic causal modeling (DCM) to further validate the
281 temporal activation sequence (see Fig. S6) and show, using a different set of assumptions
282 and method, that the temporal sequence we observe is highly likely under a set of
283 alternative sequences. We found that the most likely model is the one consistent with the
284 time course inferred from our encoding model. The DCM results provide additional
285 evidence that the temporal profile uncovered by the encoding model is a likely temporal
286 decomposition of the superimposed fMRI activations.

287 The approach we present requires that EEG and BOLD data be collected
288 simultaneously and not in separate sessions in order to exploit the correlations in trial-to-
289 trial variability to “tag” the BOLD data. To show the importance of collecting the data
290 simultaneously, we ran a control analysis that randomly permuted the trials within their

291 stimulus evidence class, thus effectively simulating an EEG and BOLD dataset collected
292 separately. By destroying the link between the EEG and BOLD trials, the encoding
293 model failed to find any consistent activation (Fig. S11/12), indicating the necessity of
294 simultaneous acquisition.

295 Alternative techniques for fusing simultaneous EEG-fMRI typically do not
296 exploit EEG across the trial and instead only analyze specific ERP components or time
297 windows of interest^{4,8,10,12-19,49,50}. Results from these techniques identify regions that
298 modulate with the specific components, but yield limited information about the timing of
299 other task-relevant regions seen in traditional fMRI contrasts. The methodology
300 developed here extends the work of Goldman, et al.¹⁷ and Walz, et al.¹⁸ by combining
301 their EEG data reduction techniques with techniques developed for encoding stimulus
302 features onto BOLD data^{20-23,36,38}, ultimately providing a framework for labeling voxels
303 in task-relevant fMRI contrasts with their timing information (Fig. S2C/E/F).

304 Clearly, other EEG components that are task-related can be isolated and could
305 potentially be used to “tag” BOLD data. The sliding window linear classification used
306 here acts to reduce the EEG data along a dimension that categorizes stimulus evidence;
307 however, this could be replaced by any other data reduction technique, such as
308 temporally windowed ICA or PCA. Variability along these component directions could
309 then be used in the encoding model to link with the simultaneously collected BOLD data.
310 The choice of data reduction technique (i.e. feature space) would be highly dependent on
311 the nature of the inferences.

312 Our methodology enabled us to observe reactivation of the pre-response network,
313 spatiotemporal dynamics that would be masked using traditional fMRI analysis.

314 Interestingly, the reactivation terminated in a network that included the MFG, SPL, and
315 IPS, similar areas previously reported to be reactivated in metacognitive judgments of
316 confidence in perceptual decisions^{42,51,52}. In addition, these areas contributed the most to
317 the correlation to confidence proxy (Fig. 7C). Gherman and Philiastides⁵³ observed this
318 network using a multivariate single-trial EEG approach, coupled with a distributed source
319 reconstruction technique. Fleming, et al.⁴² and Heereman, et al.⁵⁴ used BOLD fMRI to
320 show that areas in this network negatively correlate with subjective certainty ratings.
321 Unique to our findings, we saw this reactivation on a single-trial basis after engagement
322 of the ACC, which has been shown to be involved in decision monitoring^{53,55}, and also
323 observed the dynamic sequence leading up to this network reactivation. Our results
324 showed that reactivation/replay occurred on a trial-to-trial basis after a decision, was
325 stronger for difficult decisions, and correlated with decision confidence.

326 A potential confound in our analysis is that the timing of the reactivation overlaps
327 with some of the response times. To check if the reactivation was pre or post response,
328 we implemented a response-locked encoding model analysis (Fig. S9). The response-
329 locked results showed significant activation pre-response that overlaps with the
330 reactivation network from the stimulus locked analysis. In addition, trial-to-trial
331 reactivation taken from pre-response clusters correlates with confidence proxy similarly
332 to the stimulus locked results (Fig. S10). This provides further evidence that the
333 reactivation is occurring pre-response.

334 The encoding model we developed was able to decompose traditional fMRI
335 activation maps into their temporal order with significant voxel overlap between the
336 encoding model results and traditional results. The encoding model was also able to show

337 regions that were activated at multiple time points throughout the decision, indicating
338 temporal dynamics that were hidden previously. The regions of activation we found are
339 consistent with earlier findings; however, the work here provided the precise temporal
340 decomposition of these previously reported, temporally superimposed regions of
341 activation. In general, we have shown that simultaneously acquired EEG/fMRI data
342 enables a novel non-invasive approach to visualize high resolution spatial and temporal
343 processing in the human brain with the potential for providing a more comprehensive
344 understanding of the neural basis of complex behaviors.

345

346 ***Methods***

347 *Subjects*

348 21 subjects (12 male, 9 female; age range 20-35 years) participated in the study. The
349 Columbia University Institutional Review Board (IRB) approved all experiments and
350 informed consent was obtained before the start of each experiment. All subjects had
351 normal or corrected-to-normal vision.

352 *Stimuli*

353 We used a set of 30 face (from the Max Planck Institute face database), 30 car, and 30
354 house (obtained from the web) gray scale images (image size 512x512 pixels, 8
355 bits/pixel). They were all equated for spatial frequency, luminance, and contrast. The
356 stimulus evidence (high or low) of the task was modulated by systematically modifying
357 the salience of the image via randomization of image phase (35% (low) and 50% (high)
358 coherence)⁵⁶.

359 *Experimental task*

360 The stimuli were used in an event-related three-alternative forced choice (3-AFC) visual
361 discrimination task. On each trial, an image -- either a face, car, or house -- was presented
362 and subjects were instructed to respond with the category of the image by pressing one of
363 three buttons on an MR compatible button controller. Stimuli were presented to subjects
364 using E-Prime software (Psychology Software Tools) and a VisuaStim Digital System
365 (Resonance Technology) with 600x800 goggle display. Over four runs, a total of 720
366 trials were acquired (240 of each category with 120 high coherence trials) with a random
367 inter-trial interval (ITI) sampled uniformly between 2-2.5s. Each run lasted for 560
368 seconds.

369 *fMRI acquisition*

370 Blood-oxygenation-level-dependent (BOLD) T2*-weighted functional images were
371 acquired on a 3T Philips Achieva scanner using a gradient-echo echo-planar imaging
372 (EPI) pulse sequence with the following parameters: Repetition time (TR) 2000ms, echo
373 time (TE) 25ms, flip angle 90°, slice thickness 3mm, interslice gap 1mm, in-plane
374 resolution 3x3mm, 27 slices per volume, 280 volumes. For all of the participants, we also
375 acquired a standard T1-weighted structural MRI scan (SPGR, resolution 1x1x1mm).

376 *EEG acquisition*

377 We simultaneously and continuously recorded EEG using a custom-built MR-compatible
378 EEG system^{57,58}, with differential amplifiers and bipolar EEG montage. The caps were
379 configured with 36 Ag/AgCl electrodes including left and right mastoids, arranged as 43
380 bipolar pairs. Bipolar pair leads were twisted to minimize inductive pickup from the
381 magnetic gradient pulses and subject head motion in the main magnetic field. This
382 oversampling of electrodes ensured data from a complete set of electrodes even in

383 instances when discarding noisy channels was necessary. To enable removal of gradient
384 artifacts in our offline preprocessing, we synchronized the EEG with the scanner clock by
385 sending a transistor– transistor logic pulse at the start of each image volume. All
386 electrode impedances were kept below 20 k Ω , which included 10 k Ω resistors built into
387 each electrode for subject safety.

388 *Functional image pre-processing.*

389 Image preprocessing was performed with FSL (www.fmrib.ox.ac.uk/fsl/). Functional
390 images were spatially realigned to the middle image in the times series (motion-
391 correction), corrected for slice time acquisition, spatially smoothed with a 6mm FWHM
392 Gaussian kernel, and high pass filtered (100s). The structural images were segmented
393 (into grey matter, white matter and cerebro-spinal fluid), bias corrected and spatially
394 normalized to the MNI template using ‘FAST’⁵⁹. Functional images were registered into
395 MNI space using boundary based registration (BBR)⁶⁰.

396

397 *EEG data preprocessing.*

398 We performed standard EEG preprocessing offline using MATLAB (MathWorks) with
399 the following digital Butterworth filters: 0.5 Hz high pass to remove direct current drift,
400 60 and 120 Hz notches to remove electrical line noise and its first harmonic, and 100 Hz
401 low pass to remove high-frequency artifacts not associated with neurophysiological
402 processes. These filters were applied together in the form of a zero-phase finite impulse
403 response filter to avoid distortions caused by phase delays. We extracted stimulus-locked
404 1500 ms epochs (-500:1000) and subtracted the mean baseline – -200 ms to stimulus
405 onset – from the rest of the epoch. Through visual inspection, we discarded trials

406 containing motion and/or blink artifacts, evidenced by sudden high-amplitude
407 deflections.

408 *Sliding window logistic regression.*

409 We used linear discrimination to associate each trial with the level of stimulus evidence
410 represented in the EEG. We considered high stimulus and low stimulus evidence trials
411 irrespective of behavioral accuracy. Regularized logistic regression was used as a
412 classifier to find an optimal projection for discriminating between high and low stimulus
413 evidence trials over a specific temporal window. A sweep of the regularization
414 parameters was implemented using FaSTGLZ⁶¹. This approach has been previously
415 applied to identify neural components underlying rapid perceptual decision-making
416 ^{17,18,31,33,34,45,50,62}.

417 Specifically, we defined 50ms duration training windows centered at time, τ ,
418 ranging from stimulus onset to 800ms following the stimulus in 25ms steps. We used
419 logistic regression to estimate a spatial weighting, on N EEG channels, vector (w_τ which
420 is N x 1) that maximally discriminated between EEG sensor array signals E for each class
421 (e.g., high vs. low stimulus evidence trials):

$$422 \quad y_\tau = w_\tau^T E_\tau \quad (1)$$

423 In eqn. 1, E_τ is an N x p vector (N sensors per time window τ by p trials). For our
424 experiments, the center of the window (τ) was varied across the trial in 25ms time-steps.
425 We quantified the performance of the linear discriminator by the area under the receiver
426 operator characteristic (ROC) curve, referred to here as AUC, using a leave-one-out
427 procedure. We used the ROC AUC metric to characterize the discrimination performance
428 as a function of sliding our training window (i.e., varying τ). For each subject, this

429 produced a matrix Y where the rows corresponded to trials and the columns to training
430 windows, i.e. Y is the combination of the calculated y_{τ} for each time window.

431 *Traditional fMRI analysis.*

432 We first ran a traditional general linear model (GLM) fMRI analysis in FSL, using
433 event-related (high and low stimulus evidence) and response time (RT) variability
434 regressors. The event-related regressors comprised boxcar functions with unit amplitude
435 and onset and offset matching that of the stimuli. RT variability was modeled using the z-
436 scored RT as the amplitude of the boxcars with onset and offset matching that of the
437 stimulus, and these were orthogonalized to the event-related regressors.

438 Orthogonalization was implemented using the Gram-Schmidt procedure⁶³ to decorrelate
439 the RT regressor from all other event-related regressors. All regressors were convolved
440 with the canonical hemodynamic response function (HRF), and temporal derivatives
441 were included as confounds of no interest. An event-related high versus low stimulus
442 evidence contrast was also constructed. A fixed-effects model was used to model
443 activations across runs, and a mixed-effects approach was used to compute the contrasts
444 across subjects. Activated regions that passed a family-wise error (FWE)⁶⁴ corrected
445 cluster threshold of $p < 0.01$ at a z-score threshold of 2.57 were considered significant.

446 *fMRI deconvolution.*

447 Associating fMRI data to each trial is challenging for two main reasons: (a) the temporal
448 dynamics of the hemodynamic response function (HRF) evolve over a longer time-scale
449 than the mean ITI of the event-related design, resulting in overlapping responses between
450 adjacent trials; and (b) the ITI was random for each trial so that the fMRI data was not
451 acquired at a common lag relative to stimulus onset. To overcome these issues, we

452 employed the 'least squares - separate' (LS-S) deconvolution⁶⁵ method to estimate the
453 voxel activations for each trial. For every trial, the time series of each voxel was
454 regressed against a "signal" regressor and a "noise" regressor. The "signal" regressor was
455 the modeled HRF response due to that trial (a delta function centered at stimulus onset
456 convolved with a canonical HRF), while the "noise" regressor was the modeled HRF
457 response due to all other trials (superimposed linearly). The resulting regression
458 coefficients of the "signal" regressor represented the estimated voxel activations due to
459 that trial. These voxel activations were then organized into a single brain volume per trial.
460 We extracted 58697 voxels from a common gray matter group mask at 3 mm³ spatial
461 resolution that excluded white matter and CSF and assembled the resulting voxel
462 activations into rows of the data matrix F.

463 *Single subject encoding model.*

464 All encoding model analyses were performed in MATLAB. To relate the EEG data with
465 the fMRI, we devised a subject-wise spatio-temporal decomposition using singular value
466 decomposition (SVD). Let F be an m x p matrix denoting m-voxels and p-trials that is the
467 deconvolved high and low stimulus evidence fMRI data for each trial. Let Y be the r x p
468 matrix denoting r-windows (33 EEG_τ windows and response time (RT)) and p-trials. For
469 each trial, the first row of Y is the response times while subsequent rows are the y values
470 at each window time. Let W be an m x r matrix that is the weights on Y that solve for F.

471
$$F = WY \quad (2)$$

472 Normally, if we solve for W using the least squares approach, we get:

473
$$W=(FY^T)(YY^T)^{-1} \quad (3)$$

474 However, each time point might be highly correlated with its neighbors, which reduces
 475 the stability of the least-squares regression. We can use SVD to reduce the feature space
 476 and improve our estimation of W (the weights on each window). Then for a leave-one-
 477 out cross validation, we hold out a single trial from the EEG Y matrix and the
 478 corresponding volume from the fMRI data F and train on the remaining trials. We
 479 repeated this for all trials.

$$480 \quad Y^{\text{Train}} = U \Sigma V^T \quad (4)$$

481 Where U is an $r \times r$ orthonormal matrix, Σ is a $r \times p$ diagonal matrix and V is a $p \times p$
 482 orthonormal matrix. After SVD on Y^{Train} , we reduced the feature dimensions on Y^{Train} to
 483 retain 75% of the variance by only keeping v components. To do this, we selected the
 484 first v rows of Σ and zeroed the other rows. We now have $\tilde{\Sigma}$ as our reduced spaced
 485 matrix. If we now recalculate our least squares solution where we have replaced Y by its
 486 reduced form $U \tilde{\Sigma} V^T$ in equation 3:

$$487 \quad \hat{W} = (F^{\text{Train}} V \tilde{\Sigma}^T) (\Sigma \Sigma^T)^{-1} U^T \quad (5)$$

488 So for each leave one out fold, we first calculated the SVD of the training set. We then
 489 calculated the number of components to keep and then solve for \hat{W} , the weight estimate
 490 per fold. To test, we then applied the weights to the left-out test data Y^{Test} to estimate the
 491 encoded fMRI data \hat{F} for the encoding part:

$$492 \quad \hat{F} = \hat{W} Y^{\text{Test}} \quad (6)$$

493 While for the decoding model using the left out test data F^{Test} :

$$494 \quad \hat{Y} = \hat{W}^T F^{\text{Test}} (\hat{W}^T \hat{W})^+ \quad (7)$$

495 Here, $\hat{W}^T \hat{W}$ is not invertible, and so we used the pseudo-inverse.

496 At this point, we have \hat{F} , a $m \times p$ matrix with m voxels by p trials. For each voxel
497 j , we calculated the correlation of \hat{F}_j with F_j , resulting in the matrices R^{fMRI} (Pearson
498 Correlation Map) and P^{fMRI} (p-value map of the Pearson Correlation) that are $m \times 1$. The
499 P^{fMRI} was then converted to a z-score map. We constructed the $m \times r$ weight matrix W by
500 taking the average of all the trained \hat{W} matrices. To test which time windows were
501 significant, we also calculated, R_{τ}^{EEG} , the correlation between \hat{Y}_{τ} and Y_{τ} .

502 *Group level spatio-temporal analysis.*

503 For group level statistics, we first analyzed the R_{τ}^{EEG} vectors across all subjects. The R_{τ}^{EEG}
504 vectors were converted into their p-values, and for each time window (τ), used to
505 compute combined Stouffer p-values⁶⁶. These group level results were then false
506 discovery rate corrected (FDR) for multiple comparisons⁶⁷. To identify group level
507 voxels where our model predictions were significant, each subject's p-value maps for the
508 leave-one-out correlation were converted into their respective z-values, and voxel-wise
509 significance was calculated using threshold-free cluster enhancement (TFCE) using a
510 non-parametric randomization procedure implemented in FSL⁶⁸. Voxels were considered
511 significant if they passed a conservative false discovery rate threshold of $p < 0.01$.

512 These significant voxels were then used as a mask to temporally localize
513 activations by computing the voxels that were consistent in their direction (positive (high
514 stimulus evidence) or negative (low stimulus evidence)) and timing (τ window). To this
515 end, we implemented a spatio-temporal TFCE (stTFCE) in both space (neighboring
516 voxels) and time (neighboring time windows - response time window not included) and
517 computed significance through a randomization procedure. 33000 permutations (1000
518 permutations per window) were run by randomly altering the sign of each subject and the

519 temporal ordering of the windows, as we were testing whether the weights were
520 consistent in sign, voxel space, and temporal window. P-values were calculated by
521 comparing the true stTFCE value with the distribution of permuted values. Again, voxels
522 were considered significant if they passed FDR correction at $p < 0.05$ (high stimulus
523 evidence: FDR-Corrected $p < 0.0019$, low stimulus evidence: FDR-Corrected $p < 0.00036$).
524 Note, that now our number of multiple comparisons was the number of voxels in the
525 FDR-mask (20256) times the number of time windows (33). We analyzed the response
526 time separately with a standard TFCE randomization procedure implemented in FSL
527 (Fig. S2D).

528 *Dynamic causal modeling.*

529 To validate the encoding model timing, we implemented single-state linear
530 dynamic causal modeling (DCM) using DCM10 in SPM8⁶⁹, and applied this to the
531 BOLD data to test the hypothesis that the temporal sequence of BOLD activations we
532 found in our EEG-fMRI encoding method was most likely, relative to other possible
533 sequences of these same activations, given only the BOLD data. We used the results of
534 the encoding model to select seven regions of interest that spanned the entire trial. For the
535 first region (labeled 175 in our figures), we computed the union of activations during the
536 175ms and 200ms windows. Activations of the 225ms (225) and 250ms combined with
537 275ms (250) windows become the second and third regions. We computed the union of
538 activations during the 325ms and 350ms windows to create the fourth (325). For the fifth
539 region (400), we computed the union of the activations during the 400ms-450ms
540 windows. For the sixth region (650), we computed the union of the activations during the
541 650ms and 675ms windows. Finally, the union of the activations during the 725-800ms

542 windows was computed to create the seventh region (725). We removed any overlapping
543 voxels between any of the regions and then extracted time series from individual
544 subjects' preprocessed functional data in MNI space by estimation of the first principal
545 component within each region.

546 We constructed 11 models (Figure S6) to investigate the directed connectivity of
547 these regions and validate the temporal ordering found by the encoding model. Each
548 model was feed-forward with first node in each model as the input region. The first
549 model was the temporal ordering of the regions inferred from our EEG-fMRI encoding
550 model analysis. For five of the models, we randomized the temporal ordering of the early
551 regions (175, 225, 250) and the late regions (325, 400, 650, 725) separately. For the other
552 five models, we fully randomized the temporal ordering of all the regions.

553 We used fixed-effects Bayesian model selection (BMS) to compare these 11
554 models both on a single-subject level and at the group level. BMS balances model fit and
555 complexity, thereby selecting the most generalizable model. It estimates the relative
556 model evidence and provides a distribution of posterior probabilities for all of the models
557 considered. We also compared families of similar models⁷⁰; the model space was divided
558 into two families (early/late or fully randomized).

559

560 *Drift Diffusion Model (DDM) and Confidence Proxy.*

561 The DDM models decision-making in two-choice tasks. Here, we treated the decision
562 (correct vs. incorrect) as our two choices. A drift-process accumulates evidence over time
563 until it crosses one of two boundaries (upper or lower) and initiates the corresponding
564 response⁶⁸. The speed with which the accumulation process approaches one of the two

565 boundaries (a) is called drift-rate (v) and represents the relative evidence for or against a
566 particular response. Recently, Philiastides, et al.⁴⁵ showed that for conditions in which
567 the boundary (a) does not change, a proxy for decision confidence for each trial (i) can be
568 computed by $1 / \sqrt{RT_i - T_{non}}$.

569 We used Hierarchical Bayesian estimation of the Drift-Diffusion Model in Python
570 (HDDM) to calculate the drift rate (v), decision boundary (a) and non-decision time T_{non}
571 for each subject⁴³. Specifically, we modeled high and low stimulus evidence response
572 time data separately. This was to ensure our confidence proxies were consistent within
573 trial types. We included the response time and whether the subject got the trial correct.
574 HDDM obtains a sequence of samples (i.e., a Markov chain Monte Carlo; MCMC) from
575 the posterior of each parameter in the DDM. In our model, we generated 5000 samples
576 from the posteriors, the first 1000 (burn-in) samples were discarded, and the remaining
577 samples were thinned by 5%.

578 After modeling the DDM process, each trial's (i) confidence proxy (CP) for each
579 subject (j) was computed by $CP_{i,j} = 1 / \sqrt{RT_i - T_{non,j}}$ and then z-scored across trials where
580 $T_{non,j}$ was varied for high or low stimulus evidence trials, separately. Therefore, CP was a
581 measure of relative trial confidence within difficulty levels.

582

583 *Confidence Proxy and Decision Replay.*

584 Trial to trial reactivation amplitude was defined as $Y_{j,i}^R = W_{j,PostACC}^T F_{j,i}$ for each
585 subject (j) and trial (i), where $W_{postACC}$ is the weight matrix from the encoding model
586 thresholded by voxels that were significant in the group results from the 600-800ms

587 windows. The mean of the $Y_{j,i}^R$ across time becomes a measure of “decision replay”
588 strength for that trial (more negative y's indicate more replay activation, more positive y's
589 indicate less replay activation). $Y_{j,i}^R$ was quintiled for high and low stimulus evidence
590 and the average confidence proxy was calculated within each quintile (Fig. 7). A linear
591 mixed effects model⁷¹ was used to test if the slope of confidences across quintile
592 grouping, $Y_{j,i}^R$, were significantly different from 0 while including stimulus evidence as a
593 condition. Separate similar analyses with non-replay windows (175-250ms) and testing
594 for behavioral accuracy were also performed (Fig. S7-8). To test the contribution of each
595 cluster to the correlation with confidence, we implemented recursive feature elimination,
596 where our features were clusters of significant voxels (> 48 voxels) during the 600-
597 800ms time window. This procedure removed clusters from the ‘replay’ network before
598 calculating trial-to-trial reactivation. We then calculated the percent change in slope
599 (reactivation x confidence proxy) when the cluster was removed compared to the total
600 network. This procedure ranks cluster importance by sorting which clusters, when
601 removed, had the strongest negative effect on slope height.

602

603 ***Author Contributions***

604 Conceptualization, J.M. and P.S.; Methodology, J.M., T.R.B., J.W. B.C., R.I.G. and P.S.;
605 Investigation, J.M.; Software, J.M., B.C.; Writing – Original Draft, J.M. and P.S.; Writing
606 – Review & Editing, J.M., T.R.B., R.I.G., J.W., and P.S. ; Funding Acquisition, P.S. ;
607 Resources, J.M., T.R.B., J.W. B.C., R.I.G. and P.S.; Supervision, T.R.B and P.S.

608

609 ***Acknowledgements***

610 We would like to thank Jianing Shi for assistance in collecting the EEG/fMRI data. This
611 work was funded by National Institutes of Health Grant R01-MH085092, DARPA under
612 Contract NBCHC090029 and the Army Research Laboratory and under Cooperative
613 Agreement Number W911NF-10-2-0022.

614 **References**

- 615 1 Logothetis, N. K. What we can do and what we cannot do with fMRI. *Nature* **453**,
616 869-878, doi:10.1038/nature06976 (2008).
- 617 2 Alexander, D. M., Trengove, C. & van Leeuwen, C. Donders is dead: cortical
618 traveling waves and the limits of mental chronometry in cognitive neuroscience.
619 *Cognitive Processing*, doi:10.1007/s10339-015-0662-4 (2015).
- 620 3 Jorge, J. o., van der Zwaag, W. & Figueiredo, P. c. EEG-fMRI integration for the
621 study of human brain function. *NeuroImage* **102**, 24--34,
622 doi:10.1016/j.neuroimage.2013.05.114 (2014).
- 623 4 Huster, R. J., Debener, S., Eichele, T. & Herrmann, C. S. Methods for
624 simultaneous EEG-fMRI: an introductory review. *The Journal of neuroscience :
625 the official journal of the Society for Neuroscience* **32**, 6053-6060,
626 doi:10.1523/jneurosci.0447-12.2012 (2012).
- 627 5 Plichta, M. M. *et al.* Simultaneous EEG and fMRI Reveals a Causally Connected
628 Subcortical-Cortical Network during Reward Anticipation. *Journal of
629 Neuroscience* **33**, 14526-14533, doi:10.1523/jneurosci.0631-13.2013 (2013).
- 630 6 Yuan, H. *et al.* Negative covariation between task-related responses in alpha/beta-
631 band activity and BOLD in human sensorimotor cortex: an EEG and fMRI study
632 of motor imagery and movements. *NeuroImage* **49**, 2596-2606,
633 doi:10.1016/j.neuroimage.2009.10.028 (2010).
- 634 7 Dahne, S. *et al.* Multivariate Machine Learning Methods for Fusing Multimodal
635 Functional Neuroimaging Data. *Proceedings of the IEEE* **103**, 1507-1530,
636 doi:10.1109/JPROC.2015.2425807 (2015).
- 637 8 Warbrick, T., Arrubla, J., Boers, F., Neuner, I. & Shah, N. J. J. J. Attention to
638 Detail: Why Considering Task Demands Is Essential for Single-Trial Analysis of
639 BOLD Correlates of the Visual P1 and N1. *Journal of cognitive neuroscience* **26**,
640 1--14, doi:10.1162/jocn (2013).
- 641 9 Baumeister, S. *et al.* Sequential inhibitory control processes assessed through
642 simultaneous EEG-fMRI. *NeuroImage*, doi:10.1016/j.neuroimage.2014.01.023
643 (2014).
- 644 10 Novitskiy, N., Ramautar, J. R. & Vanderperren, K. a. The BOLD correlates of the
645 visual P1 and N1 in single-trial analysis of simultaneous EEG-fMRI recordings
646 during a spatial detection task. *NeuroImage* **54**, 824--835,
647 doi:10.1016/j.neuroimage.2010.09.041 (2010).
- 648 11 Nguyen, V. T. & Cunnington, R. The superior temporal sulcus and the N170
649 during face processing: Single trial analysis of concurrent EEG-fMRI.
650 *NeuroImage*, doi:10.1016/j.neuroimage.2013.10.047 (2013).

- 651 12 De Martino, F. *et al.* Multimodal imaging: an evaluation of univariate and
652 multivariate methods for simultaneous EEG/fMRI. *Magnetic resonance imaging*
653 **28**, 1104-1112, doi:10.1016/j.mri.2009.12.026 (2010).
- 654 13 Mayhew, S. D., Ostwald, D., Porcaro, C. & Bagshaw, A. P. Spontaneous EEG
655 alpha oscillation interacts with positive and negative BOLD responses in the
656 visual-auditory cortices and default-mode network. *NeuroImage* **76**, 362-372,
657 doi:10.1016/j.neuroimage.2013.02.070 (2013).
- 658 14 Jann, K. *et al.* BOLD correlates of EEG alpha phase-locking and the fMRI default
659 mode network. *NeuroImage* **45**, 903-916, doi:10.1016/j.neuroimage.2009.01.001
660 (2009).
- 661 15 Jaspers-Fayer, F., Ertl, M., Leicht, G., Leupelt, A. & Mulert, C. Single-trial EEG-
662 fMRI coupling of the emotional auditory early posterior negativity. *NeuroImage*
663 **62**, 1807-1814, doi:10.1016/j.neuroimage.2012.05.018 (2012).
- 664 16 Omata, K., Hanakawa, T., Morimoto, M. & Honda, M. Spontaneous Slow
665 Fluctuation of EEG Alpha Rhythm Reflects Activity in Deep-Brain Structures: A
666 Simultaneous EEG-fMRI Study. *PloS one* **8**, e66869-e66869,
667 doi:10.1371/journal.pone.0066869 (2013).
- 668 17 Goldman, R. I. *et al.* Single-trial discrimination for integrating simultaneous EEG
669 and fMRI: identifying cortical areas contributing to trial-to-trial variability in the
670 auditory oddball task. *NeuroImage* **47**, 136-147,
671 doi:10.1016/j.neuroimage.2009.03.062 (2009).
- 672 18 Walz, J. M. *et al.* Simultaneous EEG-fMRI Reveals Temporal Evolution of
673 Coupling between Supramodal Cortical Attention Networks and the Brainstem.
674 *The Journal of neuroscience : the official journal of the Society for Neuroscience*
675 **33**, 19212-19222, doi:10.1523/jneurosci.2649-13.2013 (2013).
- 676 19 Fouragnan, E., Retzler, C., Mullinger, K. & Philiastides, M. G. Two
677 spatiotemporally distinct value systems shape reward-based learning in the human
678 brain. *Nature communications* **6**, 8107, doi:10.1038/ncomms9107 (2015).
- 679 20 Naselaris, T., Kay, K. N., Nishimoto, S. & Gallant, J. L. Encoding and decoding
680 in fMRI. *NeuroImage* **56**, 400-410, doi:10.1016/j.neuroimage.2010.07.073
681 (2011).
- 682 21 Hansen, K. A., Kay, K. N. & Gallant, J. L. Topographic organization in and near
683 human visual area V4. *Journal of Neuroscience* **27**, 11896--11911,
684 doi:10.1523/JNEUROSCI.2991-07.2007 (2007).
- 685 22 Kay, K. N., Naselaris, T., Prenger, R. J. & Gallant, J. L. Identifying natural
686 images from human brain activity. *Nature* **452**, 352--355,
687 doi:10.1038/nature06713 (2008).
- 688 23 Nishimoto, S. *et al.* Reconstructing visual experiences from brain activity evoked
689 by natural movies. *Current Biology* **21**, 1641--1646,
690 doi:10.1016/j.cub.2011.08.031 (2011).
- 691 24 Silbert, L. J., Honey, C. J., Simony, E., Poeppel, D. & Hasson, U. Coupled neural
692 systems underlie the production and comprehension of naturalistic narrative
693 speech. *Proceedings of the National Academy of Sciences* **111**, E4687--E4696,
694 doi:10.1073/pnas.1323812111 (2014).

- 695 25 Horikawa, T., Tamaki, M., Miyawaki, Y. & Kamitani, Y. Neural decoding of
696 visual imagery during sleep. *Science (New York, N.Y.)* **340**, 639-642,
697 doi:10.1126/science.1234330 (2013).
- 698 26 Philiastides, M. G., Ratcliff, R. & Sajda, P. Neural representation of task
699 difficulty and decision making during perceptual categorization: a timing
700 diagram. *The Journal of neuroscience : the official journal of the Society for*
701 *Neuroscience* **26**, 8965-8975, doi:10.1523/JNEUROSCI.1655-06.2006 (2006).
- 702 27 Banko, E. M., Gal, V., Kortvelyes, J., Kovacs, G. & Vidnyanszky, Z. Dissociating
703 the effect of noise on sensory processing and overall decision difficulty. *The*
704 *Journal of neuroscience : the official journal of the Society for Neuroscience* **31**,
705 2663-2674, doi:10.1523/JNEUROSCI.2725-10.2011 (2011).
- 706 28 Erickson, D. T. & Kayser, A. S. The neural representation of sensorimotor
707 transformations in a human perceptual decision making network. *NeuroImage*
708 **79C**, 340-350, doi:10.1016/j.neuroimage.2013.04.085 (2013).
- 709 29 Heekeren, H. R., Marrett, S., Bandettini, P. a. & Ungerleider, L. G. A general
710 mechanism for perceptual decision-making in the human brain. *Nature* **431**, 859-
711 862, doi:10.1038/nature02966 (2004).
- 712 30 Philiastides, M. G. & Sajda, P. EEG-informed fMRI reveals spatiotemporal
713 characteristics of perceptual decision making. *The Journal of neuroscience : the*
714 *official journal of the Society for Neuroscience* **27**, 13082-13091,
715 doi:10.1523/JNEUROSCI.3540-07.2007 (2007).
- 716 31 Parra, L. C., Spence, C. D., Gerson, A. D. & Sajda, P. Recipes for the linear
717 analysis of EEG. *NeuroImage* **28**, 326-341,
718 doi:10.1016/j.neuroimage.2005.05.032 (2005).
- 719 32 Sajda, P., Philiastides, M. G. & Parra, L. C. Single-trial analysis of neuroimaging
720 data: inferring neural networks underlying perceptual decision-making in the
721 human brain. *IEEE Rev Biomed Eng* **2**, 97-109,
722 doi:10.1109/RBME.2009.2034535 (2009).
- 723 33 Muraskin, J., Sherwin, J. & Sajda, P. Knowing when not to swing: EEG evidence
724 that enhanced perception-action coupling underlies baseball batter expertise.
725 *NeuroImage* **123**, 1-10, doi:10.1016/j.neuroimage.2015.08.028 (2015).
- 726 34 Sherwin, J., Muraskin, J. & Sajda, P. You Can't Think and Hit at the Same Time:
727 Neural Correlates of Baseball Pitch Classification. *Frontiers in neuroscience* **6**,
728 177, doi:10.3389/fnins.2012.00177 (2012).
- 729 35 Philiastides, M. G. & Sajda, P. Temporal characterization of the neural correlates
730 of perceptual decision making in the human brain. *Cereb Cortex* **16**, 509-518,
731 doi:10.1093/cercor/bhi130 (2006).
- 732 36 Cukur, T., Nishimoto, S., Huth, A. G. & Gallant, J. L. Attention during natural
733 vision warps semantic representation across the human brain. *Nature*
734 *neuroscience* **16**, 763-770, doi:10.1038/nn.3381 (2013).
- 735 37 Naselaris, T., Kay, K. N., Nishimoto, S. & Gallant, J. L. Vol. 56 400-410
736 (2011).
- 737 38 Stansbury, D., Naselaris, T. & Gallant, J. Natural Scene Statistics Account for the
738 Representation of Scene Categories in Human Visual Cortex. *Neuron* **79**, 1025--
739 1034, doi:10.1016/j.neuron.2013.06.034 (2013).

- 740 39 Wendel, K. *et al.* EEG/MEG source imaging: methods, challenges, and open
741 issues. *Computational intelligence and neuroscience*, 656092,
742 doi:10.1155/2009/656092 (2009).
- 743 40 Friston, K. J., Harrison, L. & Penny, W. Dynamic causal modelling. *NeuroImage*
744 **19**, 1273--1302, doi:10.1016/S1053-8119(03)00202-7 (2003).
- 745 41 Deuker, L. *et al.* Memory consolidation by replay of stimulus-specific neural
746 activity. *The Journal of neuroscience : the official journal of the Society for*
747 *Neuroscience* **33**, 19373-19383, doi:10.1523/JNEUROSCI.0414-13.2013 (2013).
- 748 42 Fleming, S. M., Huijgen, J. & Dolan, R. J. Prefrontal contributions to
749 metacognition in perceptual decision making. *The Journal of neuroscience : the*
750 *official journal of the Society for Neuroscience* **32**, 6117-6125,
751 doi:10.1523/JNEUROSCI.6489-11.2012 (2012).
- 752 43 Wiecki, T. V., Sofer, I. & Frank, M. J. HDDM: Hierarchical Bayesian estimation
753 of the Drift-Diffusion Model in Python. *Frontiers in neuroinformatics* **7**, 14,
754 doi:10.3389/fninf.2013.00014 (2013).
- 755 44 Ratcliff, R. & McKoon, G. The diffusion decision model: theory and data for two-
756 choice decision tasks. *Neural Comput* **20**, 873--922, doi:10.1162/neco.2008.12-
757 06-420 (2008).
- 758 45 Philiastides, M. G., Heekeren, H. R. & Sajda, P. Human Scalp Potentials Reflect a
759 Mixture of Decision-Related Signals during Perceptual Choices. *Journal of*
760 *Neuroscience* **34**, 16877--16889, doi:10.1523/JNEUROSCI.3012-14.2014 (2014).
- 761 46 Kiani, R., Corthell, L. & Shadlen, M. N. Choice certainty is informed by both
762 evidence and decision time. *Neuron* **84**, 1329-1342,
763 doi:10.1016/j.neuron.2014.12.015 (2014).
- 764 47 Siegel, M., Buschman, T. J. & Miller, E. K. Cortical information flow during
765 flexible sensorimotor decisions. *Science* **348**, 1352-1355,
766 doi:10.1126/science.aab0551 (2015).
- 767 48 Gold, J. I. & Shadlen, M. N. The neural basis of decision making. *Annual review*
768 *of neuroscience* **30**, 535-574, doi:10.1146/annurev.neuro.29.051605.113038
769 (2007).
- 770 49 Warbrick, T. *et al.* Single-trial P3 amplitude and latency informed event-related
771 fMRI models yield different BOLD response patterns to a target detection task.
772 *NeuroImage* **47**, 1532-1544, doi:10.1016/j.neuroimage.2009.05.082 (2009).
- 773 50 Walz, J. M. *et al.* Simultaneous EEG-fMRI reveals a temporal cascade of task-
774 related and default-mode activations during a simple target detection task.
775 *NeuroImage* **102 Pt 1**, 229-239, doi:10.1016/j.neuroimage.2013.08.014 (2014).
- 776 51 Yeung, N. & Summerfield, C. Metacognition in human decision-making:
777 confidence and error monitoring. *Philosophical transactions of the Royal Society*
778 *of London. Series B, Biological sciences* **367**, 1310-1321,
779 doi:10.1098/rstb.2011.0416 (2012).
- 780 52 Steihauser, M. & Yeung, N. Decision processes in human performance
781 monitoring. *The Journal of neuroscience : the official journal of the Society for*
782 *Neuroscience* **30**, 15643-15653, doi:10.1523/JNEUROSCI.1899-10.2010 (2010).
- 783 53 Gherman, S. & Philiastides, M. G. Neural representations of confidence emerge
784 from the process of decision formation during perceptual choices. *NeuroImage*
785 **106**, 134-143, doi:10.1016/j.neuroimage.2014.11.036 (2015).

- 786 54 Heereman, J., Walter, H. & Heekeren, H. R. A task-independent neural
787 representation of subjective certainty in visual perception. *Front Hum Neurosci* **9**,
788 551, doi:10.3389/fnhum.2015.00551 (2015).
- 789 55 Botvinick, M. M., Braver, T. S., Barch, D. M., Carter, C. S. & Cohen, J. D.
790 Conflict monitoring and cognitive control. *Psychological review* **108**, 624-652
791 (2001).
- 792 56 Dakin, S. C., Hess, R. F., Ledgeway, T. & Achtman, R. L. What causes non-
793 monotonic tuning of fMRI response to noisy images? *Current biology : CB* **12**,
794 R476-477; author reply R478 (2002).
- 795 57 Sajda, P., Goldman, R. I., Dyrholm, M. & Brown, T. R. *Signal Processing and*
796 *Machine Learning for Single-trial Analysis of Simultaneously Acquired EEG and*
797 *fMRI*. (Elsevier Inc., 2010).
- 798 58 Sajda, P., Goldman, R. I., Philiastides, M. G., Gerson, A. D. & Brown, T. R. A
799 System for Single-trial Analysis of Simultaneously Acquired EEG and fMRI.
800 *2007 3rd International IEEE/EMBS Conference on Neural Engineering*,
801 doi:10.1109/CNE.2007.369667 (2007).
- 802 59 Zhang, Y., Brady, M. & Smith, S. Segmentation of brain MR images through a
803 hidden Markov random field model and the expectation-maximization algorithm.
804 *IEEE transactions on medical imaging* **20**, 45--57, doi:10.1109/42.906424 (2001).
- 805 60 Greve, D. N. & Fischl, B. Accurate and robust brain image alignment using
806 boundary-based registration. *NeuroImage* **48**, 63--72,
807 doi:10.1016/j.neuroimage.2009.06.060 (2009).
- 808 61 Conroy, B. R., Walz, J. M. & Sajda, P. Fast bootstrapping and permutation testing
809 for assessing reproducibility and interpretability of multivariate fMRI decoding
810 models. *PloS one* **8**, e79271, doi:10.1371/journal.pone.0079271 (2013).
- 811 62 Sherwin, J. & Sajda, P. Musical experts recruit action-related neural structures in
812 harmonic anomaly detection: evidence for embodied cognition in expertise. *Brain*
813 *and Cognition* **83**, 190-202, doi:10.1016/j.bandc.2013.07.002 (2013).
- 814 63 Strang, G. Introduction to Linear Algebra. *Mathematics of Computation* **18**, 510,
815 doi:10.2307/2003783 (2003).
- 816 64 Nichols, T. & Hayasaka, S. Controlling the familywise error rate in functional
817 neuroimaging: a comparative review. *Statistical methods in medical research* **12**,
818 419--446, doi:10.1191/0962280203sm341ra (2003).
- 819 65 Mumford, J. A., Turner, B. O., Ashby, F. G. & Poldrack, R. A. Deconvolving
820 BOLD activation in event-related designs for multivoxel pattern classification
821 analyses. *NeuroImage* **59**, 2636-2643, doi:10.1016/j.neuroimage.2011.08.076
822 (2012).
- 823 66 Darlington, R. B. & Hayes, A. F. Combining independent p values: extensions of
824 the Stouffer and binomial methods. *Psychological methods* **5**, 496-515,
825 doi:10.1037/1082-989X.5.4.496 (2000).
- 826 67 Benjamini, Y. & Hochberg, Y. Controlling the False Discovery Rate: A Practical
827 and Powerful Approach to Multiple Testing. *Journal of the Royal Statistical*
828 *Society. Series B (Methodological)* **57**, 289 -- 300, doi:10.2307/2346101 (1995).
- 829 68 Smith, S. M. & Nichols, T. E. Threshold-free cluster enhancement: addressing
830 problems of smoothing, threshold dependence and localisation in cluster
831 inference. *NeuroImage* **44**, 83-98, doi:10.1016/j.neuroimage.2008.03.061 (2009).

- 832 69 Stephan, K. E. *et al.* Ten simple rules for dynamic causal modeling. *NeuroImage*
833 **49**, 3099--3109, doi:10.1016/j.neuroimage.2009.11.015 (2010).
834 70 Penny, W. D. *et al.* Comparing families of dynamic causal models. *PLoS*
835 *Computational Biology* **6**, doi:10.1371/journal.pcbi.1000709 (2010).
836 71 Bates, D., Mächler, M., Bolker, B. & Walker, S. Fitting Linear Mixed-Effects
837 Models Using lme4. *2015* **67**, 48, doi:10.18637/jss.v067.i01 (2015).
838
839

840

841 **Figure Captions**

842 **Figure 1. Paradigm and traditional EEG and fMRI results**

843 **A**, 3-AFC task where stimulus evidence for each category is modulated by varying the
844 phase coherence in the images. **B**, Example of face images with high stimulus evidence
845 (high coherence: 50%) and low stimulus evidence (low coherence: 35%). **C**, Behavioral
846 performance shows significant differences, as a function of stimulus evidence, in
847 accuracy ($p < 10^{-12}$, paired t-test) and **D**, response time ($p < 10^{-8}$, paired t-test) across the
848 group. **E**, Grand average stimulus-locked event related potentials (ERPs) for electrode Pz
849 show that differences in stimulus evidence span the time from stimulus to response. **F**,
850 fMRI analysis showing cortical areas correlated with high (red) vs. low (blue) stimulus
851 evidence across the entire trial ($Z > 2.57$ with $p < 0.01$ Family-Wise Error cluster
852 corrected).

853 **Figure 2. Temporally precise trial-to-trial EEG variability tags brain regions during**
854 **decision-making**

855 **A**, Illustration of how trial-to-trial variability of neural activity in spatially distinct
856 cortical areas can be used to tag brain regions. In this hypothetical example Region 1 is
857 involved in sensory encoding while Region 2 integrates sensory evidence to form a
858 decision (in NHP literature, Region 1 might represent MT, while Region 2 LIP). Neural
859 activity across the trial is shown for two stimulus types, one with high sensory evidence
860 for the choice (red curves) and one with low sensory evidence (blue curves). Also
861 shown are two temporal windows (τ_1 and τ_2) that represent different times during the
862 trial. **B**, Linear classifiers are trained to separate trials based on the two levels of stimulus
863 evidence at specific temporal windows. Shown are classifiers (parameterized by weight

864 vectors w_1 and w_2) for two temporal windows (τ_1 and τ_2) with respect to two EEG sensors
865 (for simplicity only two dimensions of the full $N=43$ sensor space are shown. Though
866 the component hyperplane is optimal for the full 43 dimensions, when projected to a line
867 in two dimensions for illustration, it may appear that the separation is sub-optimal). This
868 yields an EEG discriminant component for each temporal window. Variability along
869 these components serves as a unique feature vector for temporally tagging the BOLD
870 data—e.g. variability along an EEG component trained with data from τ_1 tags BOLD
871 voxels with time τ_1 while variability along an EEG component trained with data from τ_2
872 tags them with τ_2 .

873

874 **Figure 3. Encoding models based on stimulus derived features versus EEG**
875 **variability**

876 **A**, A traditional encoding model used in fMRI analysis extracts a set of features from the
877 stimulus that are potentially representative of low level structure and high level semantics
878 (green box). Weights are learned to model how these stimulus features are encoded in
879 the fMRI BOLD signal. The resulting encoding model is used to make predictions based
880 on how well different voxels predict the features from novel stimuli. For example, one
881 can create maps of the brain that are labeled based on the stimulus features that each
882 voxel represents. **B**, The same encoding model concept applied to EEG variability (EEG
883 encoding model). Instead of features being estimated from the stimulus, they are derived
884 from EEG component trial-to-trial variability (as in Fig 2a) with each temporal window
885 representing a different feature (green box). Weights are learned so as to model how the
886 EEG variability at a given time window is encoded in the fMRI BOLD. As in the

887 traditional encoding model, predictions on novel stimuli can be done to test the model
888 and results can be used to construct a map—in this case a map of the brain that shows
889 the timing of the EEG component variability that each voxels represents.

890

891 **Figure 4. EEG discrimination and encoding model results**

892 **A**, Group average area under the receiver operating curve (AUC) for the sliding window
893 logistic regression EEG discrimination analysis, comparing high versus low stimulus
894 evidence trials; standard error across subjects is shown with shading. **B**, A single subject's
895 discriminating y-value distributions for high (red) and low stimulus evidence (blue) trials
896 for two EEG time points (225ms and 600ms). **C**, Significant fMRI voxels resulting from
897 the group level analysis for the encoding model ($p < 0.01$ TFCE-False Discovery Rate
898 (FDR) corrected). Activity is seen encompassing early visual processing regions,
899 attention networks, and the task positive network. **D**, A random subset of 100 (50 for
900 each stimulus evidence condition) from 700 total trials of the actual (circle) and predicted
901 (diamond) BOLD responses from the encoding model, for an example subject at a single
902 voxel (MNI X/Y/Zmm: -27/-54/-15, $r=0.206$, $p < 10^{-6}$). High and low stimulus evidence
903 trials are shown separately for clarity. **E**, The averaged correlation of the predicted y-
904 values with the true y-values across the trial duration. Blue shading represents the
905 standard error across subjects. Grey shading indicates significant time windows ($p < 0.05$
906 FDR-corrected).

907

908 **Figure 5. Group-level encoding model weights results show neural activation cascade**

909 Subset of thresholded ($p < 0.05$ FDR-Corrected, $k=10$) group level statistical parametric
910 maps created by stTFCE randomization procedure on the encoding model weight
911 matrices show the progression of spatial activity across the trial. Activation can be seen
912 early in the trial in the occipital regions while progressing more anteriorly later in the trial
913 to executive control areas. Activations in red indicate areas where high stimulus evidence
914 trials had larger activations than low stimulus evidence trials, and blue the inverse.

915

916 **Figure 6. Spatial-temporal event-related activations show coordinated reactivations.**

917 **A**, Union across time windows of significant voxels for high (red) and low (blue)
918 stimulus evidence activations. Voxels with activations for both high and low conditions
919 (at different time windows) are displayed in green. Also shown are the encoding model
920 weights for specific voxels, including fusiform gyrus (FG-R):36/-51/-18, (FG-L):-42/-
921 42/-18, superior lateral occipital cortex (sLOC):24/-63/36, superior parietal lobule
922 (SPL):27/-51/54, anterior cingulate cortex (ACC):-6/24/30, intraparietal sulcus (IPS):-
923 30/-60/39, middle frontal gyrus (MFG):-45/27/30, middle temporal gyrus (MT):-57/-
924 60/0. Asterisks indicate significant windows. **B**, Sequence of significant weights showing
925 a “replay” of the network after the onset of ACC activation (shaded ellipse). “Replay” is
926 faster than the initial stimulus driven sequence and strongest for low evidence trials.
927

928 **Figure 7. Trial-to-trial reactivation correlates with decision confidence.**

929 Trial-to-trial reactivation amplitude ($Y_{j,i}^R$ – see Methods) of “replay” correlates with
930 confidence proxy for both high (**A**) and low (**B**) stimulus evidence conditions. Error bars
931 represent standard errors across subjects. (**C**), Stimulus-locked replay activation clusters

932 and feature importance. **(inset)** Regions of interest used in computing the reactivation
933 values for computing confidence proxy correlations. These regions were taken from
934 significant group activations from 600-800ms post stimulus. Regions were then clustered
935 (> 48 voxels) and a secondary analysis for feature importance was performed. Here, we
936 removed each cluster before computing trial-to-trial reactivations and compared the slope
937 of reactivation x confidence proxy when all clusters were present. Panel C shows the
938 ranking of feature importance for each cluster (more negative % change = more
939 importance). Negative changes in slopes show that by removing that cluster the slope of
940 the correlation between reactivation and confidence decreases, indicating the importance
941 of that cluster. Increases in slope indicate that the correlation is higher with that region
942 removed.

943 **Figures:**

944

945

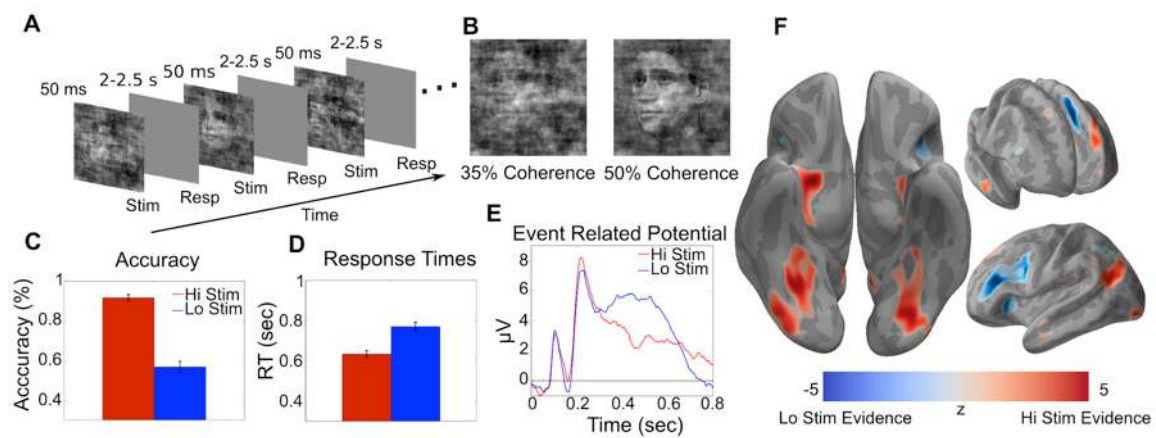
946

947

948

949

950



951

952 *Figure 1.*

953

954

955

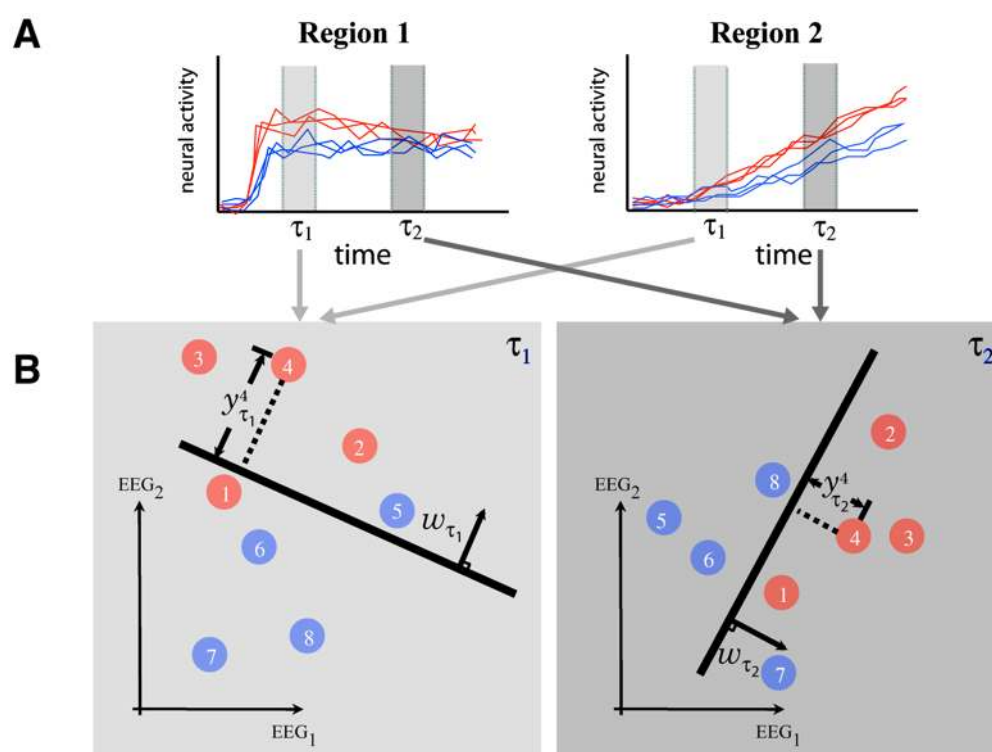
956

957

958

959

960



961

962 *Figure 2.*

963

964

965

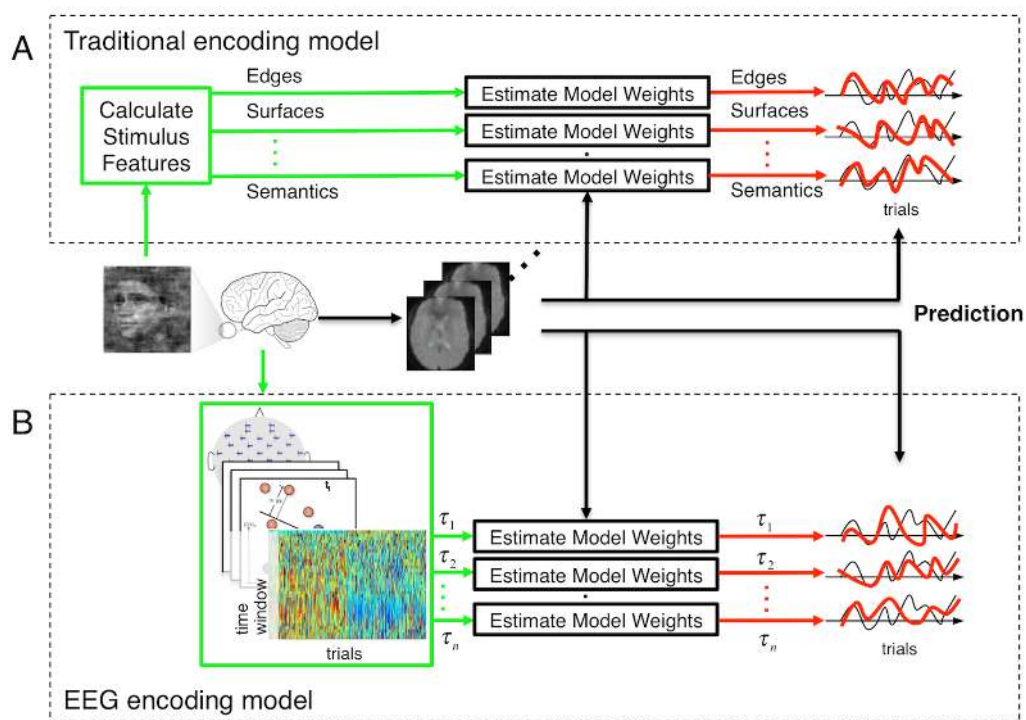
966

967

968

969

970



971

972 *Figure 3.*

973

974

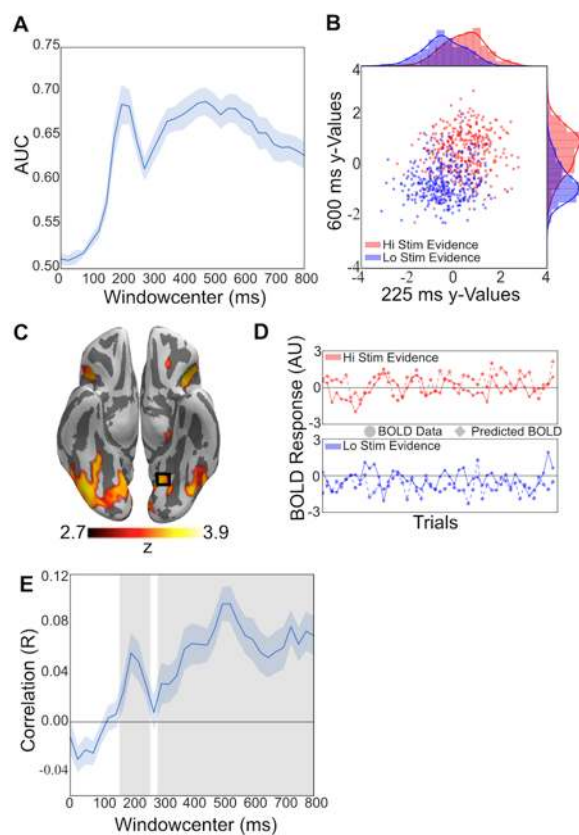
975

976

977

978

979



980

981 *Figure 4.*

982

983

984

985

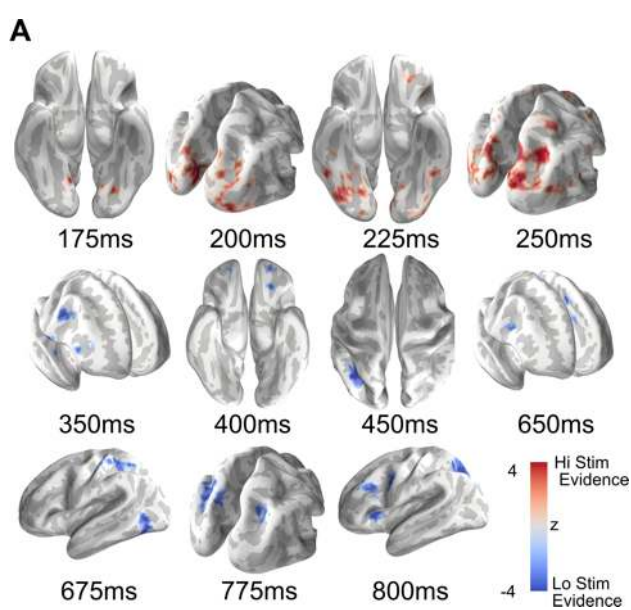
986

987

988

989

990



991

992 *Figure 5.*

993

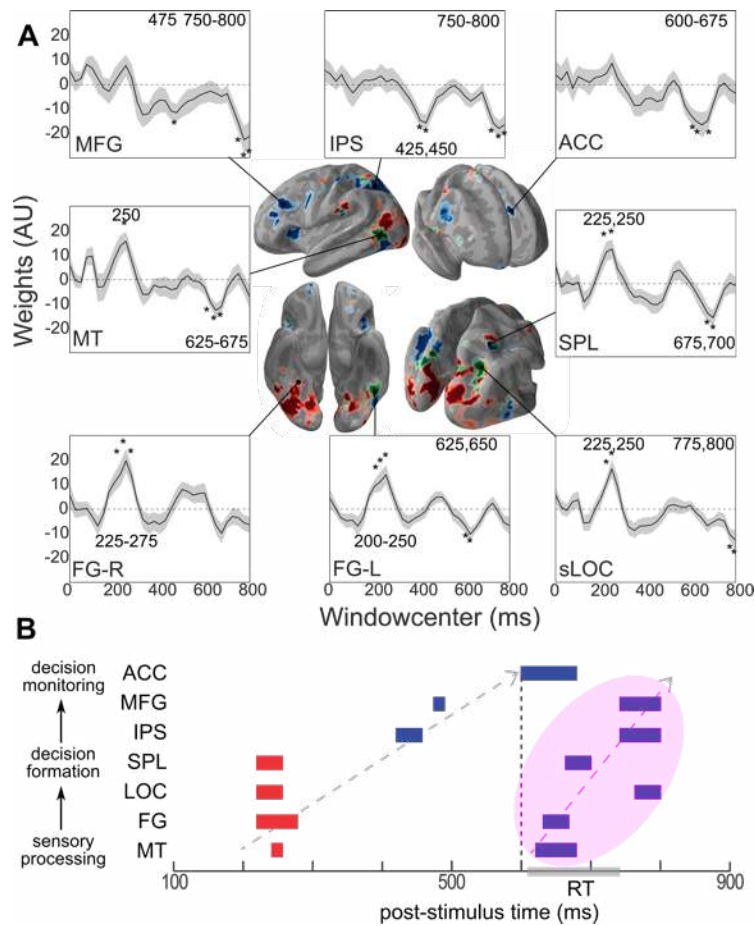
994

995

996

997

998



999

1000 *Figure 6.*

1001

1002

1003

1004

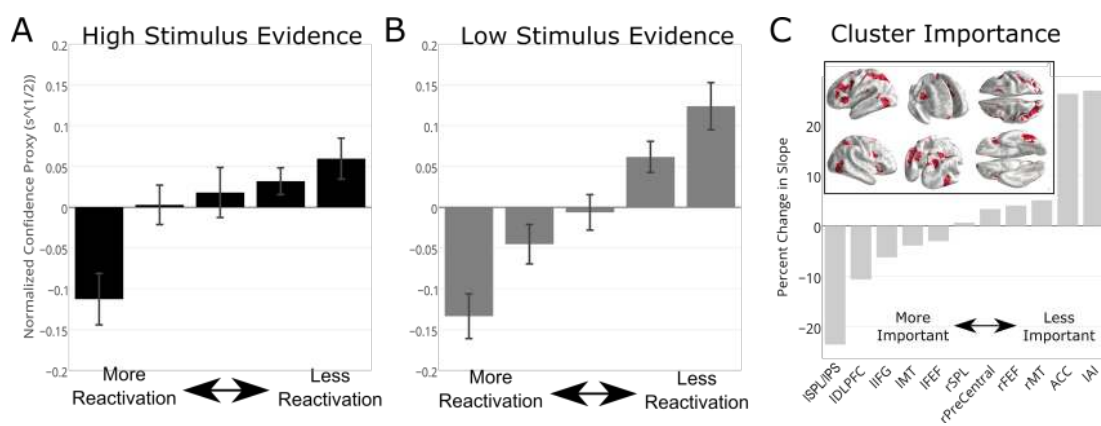
1005

1006

1007

1008

1009



1010

1011 *Figure 7.*